Towards predictive many-body calculations of phonon-limited carrier mobilities in semiconductors

Supplemental Material

Samuel Poncé,[1] Elena R. Margine,[2] and Feliciano Giustino[1,*]

[1] *Department of Materials, University of Oxford, Parks Road, Oxford, OX1 3PH, UK*
[2] *Department of Physics, Binghamton University-SUNY, Binghamton, New York 13902, USA*

(Dated: March 14, 2018)

Computational Methods

In this work we use norm-conserving pseudopotentials with planewave kinetic energy cutoffs of 45 Ry and 35 Ry for LDA and PBE calculations, respectively. The phonon dispersion relations are evaluated using density-functional perturbation theory [1], starting from a 6×6×6 uniform grid of **q**-points. An 18×18×18 uniform grid of **k**-points was required to correctly obtain vanishing Born effective charges. Representative phonon dispersion relations obtained within this setup can be found in Ref. [2]. The coarse grids for the electron-phonon interpolation required 12×12×12 **k**-points and 6×6×6 **q**-points. Such a dense **k**-grid was needed to obtain a good Wannier interpolation of the conduction bands, since the minimum is along the Δ line (approx. 0.85ΓX) and does not fall on a high-symmetry point.

For the self-consistent, iterative solution of the Boltzmann transport equation (IBTE) we employ uniform Brillouin-zone grids, and the **q**-point sums are restricted to the irreducible wedge of the Brillouin zone using crystal symmetry operations. The IBTE is solved using homogeneous and commensurate **k**- and **q**-point grids since the variations $\partial_{E_\beta} f^{i+1}_{n\mathbf{k}}$ at the $(i+1)$-th iteration require the knowledge of the variations $\partial_{E_\beta} f^{i}_{n\mathbf{k}+\mathbf{q}}$ at the i-th iteration, see Eq. (2) of the main text.

For the direct solution of the BTE within the self-energy relaxation time approximation (SERTA) the Brillouin zone grids do not need to be commensurate. In this case, in order to improve the sampling accuracy, we employ quasi-random Sobol sequences of **k**- and **q**-points. Following recommended practice, we skip the first 1000 elements of a sequence and we retain one element every 100 of the remainder [3]; furthermore we employ a linear scramble and shift of the resulting sequence, using standard routines from `Matlab R2015a` [4]. As a further refinement we replace the homogeneous Sobol weights using a Voronoi triangulation with the code `Voro++` [5]. In the Voronoi triangulation we take into account the periodicity of the Brillouin zone by building periodic replicas of the random grid in neighboring reciprocal unit cells. For the **k**-point grid we also densify the distribution around the band extrema, in order to capture the fine features of the scattering near the band edges. This is achieved by generating additional random points with the Lorentz distribution $1/(1+|\mathbf{k}-\mathbf{k}_0|^2/\gamma^2)$ and by recomputing the Voronoi weights of the resulting grid. Here $\mathbf{k}_0$ indicates the location of the band extrema and $\gamma = 0.008$ Å^{-1}.

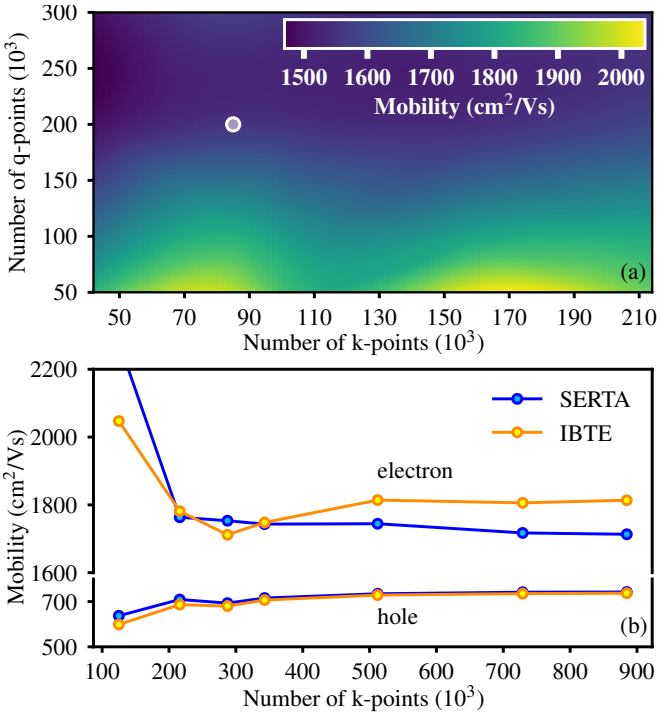

FIG. S1. (a) Sensitivity of the intrinsic electron mobility of silicon at 300 K with respect to the sampling of electron (**k**) and phonon (**q**) wavevectors in the Brillouin zone. The calculations are performed within the SERTA approximation, using a densified Lorentzian distribution of **k**-points around the conduction band minima, and a Sobol quasi-random sampling of the **q**-points. The white dot indicates the setup used in the calculations reported in the main text of this article. (b) Comparison between the rate of convergence of the intrinsic electron and hole mobilities of silicon using the SERTA and the IBTE approaches, at 300 K. In this case we use uniform grids, with the **k**-point mesh being twice as dense as the **q**-point mesh in each direction.

Figure S1(a) shows the convergence of the intrinsic mobility of silicon at 300 K with respect to the number of electron and phonon wavevectors in the Brillouin zone within the SERTA approximation. Figure S1(b) shows the comparison between calculations of the intrinsic mo-

bility of silicon within the SERTA and the IBTE approaches.

The GW calculations are performed starting from the PBE band structure and using the experimental lattice parameters on a 12×12×12 **k**-point grid. To obtain direct and indirect band gaps converged to within 5 meV we use 120 bands and a planwaves cutoff of 15 Ry for the dielectric matrix. The renormalization of the band velocity is evaluated as in Ref. [6]: $\langle\psi_{n\mathbf{k}}|\hat{\mathbf{p}}|\psi_{m\mathbf{k}}\rangle_{\mathrm{GW}} = [(\varepsilon^{\mathrm{GW}}_{n\mathbf{k}} - \varepsilon^{\mathrm{GW}}_{m\mathbf{k}})/(\varepsilon^{\mathrm{DFT}}_{n\mathbf{k}} - \varepsilon^{\mathrm{DFT}}_{m\mathbf{k}})]\langle\psi_{n\mathbf{k}}|\hat{\mathbf{p}}|\psi_{m\mathbf{k}}\rangle_{\mathrm{DFT}}$, where $\hat{\mathbf{p}}$ indicates the momentum operator. When $n = m$ the previous expression is replaced by $\langle\psi_{n\mathbf{k}}|\hat{\mathbf{p}}|\psi_{n\mathbf{k}}\rangle_{\mathrm{GW}} = \langle\psi_{n\mathbf{k}}|\hat{\mathbf{p}}|\psi_{n\mathbf{k}}\rangle_{\mathrm{DFT}}$.

For completeness the effective masses computed within scalar-relativistic DFT, fully-relativistic DFT, and including GW quasiparticle corrections are reported in Table S1. We also show in Table S2 the effective masses calculated without SOC at the experimental lattice parameter with two different types of pseudization (norm-conserving and ultrasoft), and two exchange and correlation functionals (LDA and PBE).

In order to calculate mobilities using band structures as close as possible to experiments (i.e. the lowermost bars in Fig. 1), we repeated the calculations using the low-energy dispersion relations parametrized in Refs. 7 and 8 starting from the measured effective masses:

$$\varepsilon_{\mathrm{cb}} = \frac{\hbar^2(k_x - k_{0,x})^2}{2m_{||}} + \frac{\hbar^2(k_y - k_{0,y})^2}{2m_{\perp}} + \frac{\hbar^2(k_z - k_{0,z})^2}{2m_{\perp}} + \varepsilon_{\mathrm{c}}, \quad (1)$$

$$\varepsilon_{\mathrm{hh}} = Ak^2 + [B^2k^4 + C^2(k_x^2k_y^2 + k_y^2k_z^2 + k_z^2k_x^2)]^{1/2}, \quad (2)$$

$$\varepsilon_{\mathrm{lh}} = Ak^2 - [B^2k^4 + C^2(k_x^2k_y^2 + k_y^2k_z^2 + k_z^2k_x^2)]^{1/2}, \quad (3)$$

$$\varepsilon_{\mathrm{so}} = -\frac{k^2\hbar^2}{2m_{\mathrm{so}}} - \varepsilon_{\mathrm{so}}, \quad (4)$$

where $m_{||} = 0.98m_0$ (m_0 is the free electron mass), $m_{\perp} = 0.19m_0$, $m_{\mathrm{so}} = 0.23m_0$, $\mathbf{k}_0$ denotes the wavevectors of the conduction band minima, and ε_{c} is the conduction band bottom. The coefficients are $A = -4.1\,\hbar^2/2m_0$, $B = -1.6\,\hbar^2/2m_0$ and $C = 3.3\,\hbar^2/2m_0$ [7, 8] and $\varepsilon_{\mathrm{so}} = 48$ meV.

Broadening of Dirac delta functions

The numerical evaluation of phonon-limited mobilities using Eqs. (2)-(4) of the main text requires one to replace the Dirac delta functions in Eqs. (2)-(3) by Lorentzian functions with finite broadening η: $\pi\,\delta(\varepsilon_{n\mathbf{k}} \pm \hbar\omega_{\mathbf{q}\nu} - \varepsilon_{m\mathbf{k}+\mathbf{q}}) \to \mathrm{Im}\,(\varepsilon_{n\mathbf{k}} \pm \hbar\omega_{\mathbf{q}\nu} - \varepsilon_{m\mathbf{k}+\mathbf{q}} - i\eta)^{-1}$. This procedure makes the calculated mobility dependent on the broadening parameter, hence it is important to check how sensitive are the results to the choice of η.

Band	Direction	Present calculations			Expt.
		No SOC	SOC	SOC+GW	
Split-off hole	[100]	0.167	0.224	0.226	0.23
	[111]	0.094	0.227	0.227	0.23
	[110]	0.106	0.227	0.225	0.23
Light hole	[100]	0.253	0.189	0.202	0.17
	[111]	0.682	0.131	0.132	0.16
	[110]	0.266	0.140	0.140	0.16
Heavy hole	[100]	0.271	0.256	0.243	0.46
	[111]	0.694	0.654	0.643	0.56
	[110]	2.868	0.521	0.512	0.53
Electron	long.	0.798	0.824	1.090	0.98
	trans.	0.188	0.190	0.186	0.19

TABLE S1. Comparison between calculated and measured effective masses of silicon, in units of the electron mass. The experimental data are from Refs. 8–10.

Band	Direction	LDA-US	LDA	PBE	Expt.
Split-off hole	[100]	0.170	0.168	0.167	0.23
	[111]	0.098	0.098	0.094	0.23
	[110]	0.111	0.109	0.106	0.23
Light hole	[100]	0.248	0.265	0.253	0.17
	[111]	0.551	0.655	0.682	0.16
	[110]	0.271	0.278	0.266	0.16
Heavy hole	[100]	0.271	0.276	0.271	0.46
	[111]	0.635	0.678	0.694	0.56
	[110]	2.158	2.170	2.868	0.53
Electron	long.	0.755	0.735	0.771	0.98
	trans.	0.182	0.185	0.188	0.19

TABLE S2. Comparison between effective masses calculated using different types of pseudopotentials and exchange-correlation functionals without SOC, in units of the electron mass. The experimental data are from Refs. 8–10.

Figure S2(a) shows the intrinsic electron mobility of silicon at 0 K, evaluated as a function of η. From this figure we see that the mobility tends to diverge towards $+\infty$ as $\eta \to 0$. This trend can be rationalized by noting that the mobility is directly proportional to the relaxation time [cf. Eq. (5) of main text], and the relaxation time due to acoustic phonon scattering in a non-polar semiconductor is inversely proportional to the temperature [11]. As a result, we expect that the phonon-limited mobility will increase indefinitely as η becomes smaller and the Lorentzian approaches the Dirac delta function. This observation is in agreement with the explicit calculations in Fig. S2(a).

This behavior poses a problem when one has to decide which broadening parameter to use in the calculations. As a general rule here we set η to the smallest possible value where the curve μ vs. η is relatively flat, so

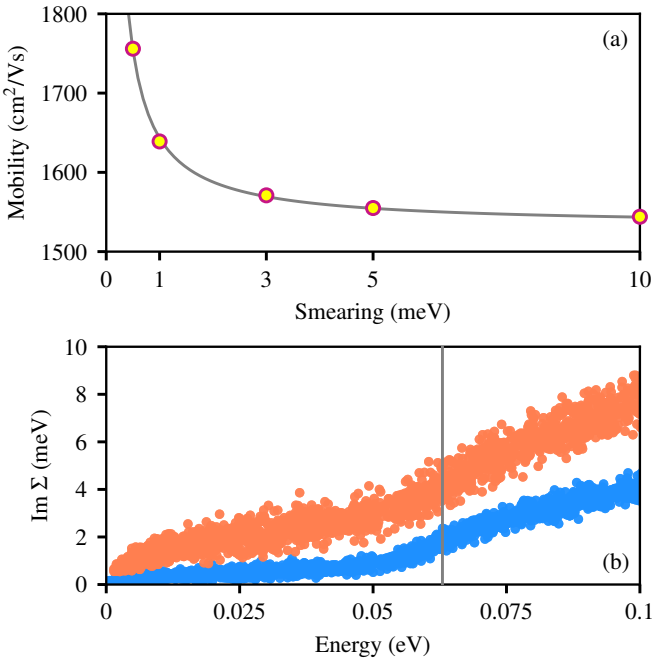

FIG. S2. (a) Intrinsic electron mobility of silicon at 0 K, calculated as a function of the broadening parameter η (dots). The grey thin line is a guide to the eye and was obtained by fitting the data points using $\mu = \text{const}/\eta$. (b) Electron quasiparticle linewidths in silicon arising from the electron-phonon interaction, calculated at 0 K (blue dots) and 300 K (orange dots). The zero of the horizontal energy axis is set to the conduction band minimum. The vertical grey line indicates the energy of the highest optical phonon in silicon.

that our results are insensitive to this choice. Based on Fig. S2(a), we use $\eta = 5$ meV in all calculations presented in the article. This choice is consistent with the notion that real quasiparticles do not have an infinite lifetime as it is assumed in the BTE formalism, but have a finite lifetime due to electron-electron and electron-phonon interactions. In Fig. S2(b) we show our calculated quasiparticle broadening from electron-phonon interactions at 0 K and 300 K. It can be seen that at 300 K the broadening reaches values up to 4-5 meV for quasiparticle energies located one phonon energy away from the band bottom (the highest phonon energy in silicon is ∼63 meV). These values are consistent with our choice of broadening parameter.

Screening of the electron-phonon matrix elements

The strategy that we used to correct for the DFT overscreening of the electron-phonon matrix elements consists of un-screening the matrix elements via the DFT dielectric function, so as to obtain the bare matrix elements, and then screening the bare matrix elements using the best possible dielectric function. The dielectric function can be factored out of the integral in the matrix element

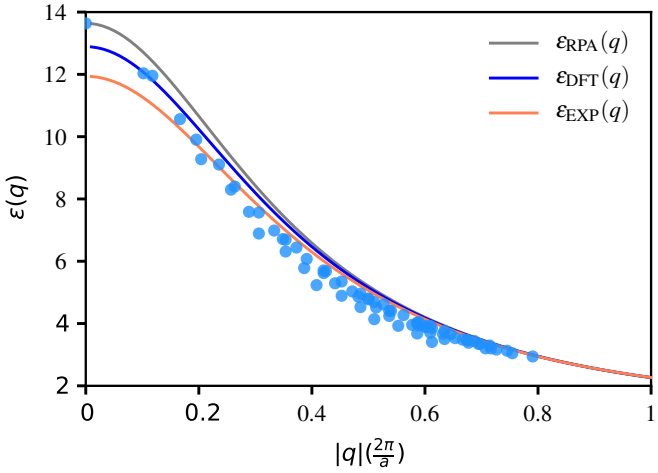

FIG. S3. Comparison between the diagonal part of the RPA dielectric matrix of silicon (blue dots) and the Thomas-Fermi model of Ref. 13 (grey line). We also show the model dielectric function using the DFT dielectric constant $\varepsilon(0) = 12.89$ (blue line) and experimental dielectric constant $\varepsilon(0) = 11.94$ (orange line).

if we neglect local field effects. Since local field effects are known to decrease the head of the dielectric function of silicon by 10% and the body of the dielectric function is typically one or two orders of magnitude smaller than the head [12], we expect to make an error on the order of a few percent.

In order to perform this operation for a large number of phonon wavevectors we use the Thomas-Fermi model dielectric function of Ref. 13:

$$\epsilon(q) = \frac{k_0^2 + q^2}{k_0^2 \sin(qR)/(qR\,\epsilon_0) + q^2}, \tag{5}$$

where $q = |\mathbf{q}|$, ϵ_0 is the macroscopic (electronic) dielectric constant. k_0 are R are obtained from the valence electron density ρ as $k_0^2 = 4(3\pi^2\,\rho)^{1/3}/\pi$ and $\sinh(k_0 R)/k_0 R = \epsilon_0$. The only free parameter of the model is ϵ_0.

We test the validity of this model by computing the dielectric matrix within the random phase approximation (RPA), using a 12×12×12 unshifted grid (corresponding to 72 inequivalent wavevectors). Figure S3 shows a comparison between the model dielectric function of Eq. (5) and the RPA calculation, after matching ϵ_0 to the head of the RPA dielectric matrix. We see that Eq. (5) reproduces well the RPA screening, therefore it is sensible to use it in the renormalization of the electron-phonon matrix elements. In this work we renormalized the matrix elements by setting ϵ_0 to the experimental dielectric constant of silicon (11.94).

Brooks-Herring model for impurity scattering

In order to account for impurity scattering in Fig. 3(b) of the main text, we use the semi-empirical model developed by Brooks and Herring [14, 15]. In this model the mobility $\mu_{\rm i}$ is evaluated analytically by taking into account quantum-mechanical scattering rates, spherical energy surfaces, negligible electron-electron interactions, and complete ionization of the impurities. The explicit expression of the hole mobility is:

$$\mu_{\rm i} = \frac{2^{7/2}\epsilon_s^2 (k_{\rm B}T)^{3/2}}{\pi^{3/2} e^3 \sqrt{m_d^*}\, n_{\rm i} G(b)} \quad \left[\frac{\rm cm^2}{\rm Vs}\right], \tag{6}$$

where $G(b) = \ln(b+1) - b/(b+1)$, $b = 24\pi m_d^* \epsilon_s (k_{\rm B}T)^2/e^2h^2n'$, and $n' = n_{\rm h}(2 - n_{\rm h}/n_{\rm i})$. Here $m_d^* = 0.55 m_0$ is the density-of-state effective mass for the holes [16], $n_{\rm h}$ and $n_{\rm i}$ are the hole densities and the density of ionized impurities [impurity concentration in Fig. 3(b) of the main text], respectively, $\epsilon_s = 11.9\epsilon_0$ is the dielectric constant, ϵ_0 is the permittivity of vacuum, and h is Planck's constant. In the above expressions, the concentrations are expressed in $\rm cm^{-3}$, and the temperature T is in K.

In the case of silicon, Eq. (6) cannot be used for the electron mobility because the electron mass is highly anisotropic and leads to incorrect results. To account for the electron mass anisotropy, we instead used the Long-Norton mobility expression [15, 17]:

$$\mu_{\rm i}^{\rm LN} = \frac{7.3 \cdot 10^{17} T^{3/2}}{n_i G(b)} \quad \left[\frac{\rm cm^2}{\rm Vs}\right], \tag{7}$$

where the electron density-of-state effective mass is $m_d^* = 1.08 m_0$ [10].

Finally, the mobility including phonon (μ_l) and impurity (μ_i) scattering can be computed using the mixed-scattering formula [15]:

$$\mu = \mu_l \left[1 + X^2 \{ {\rm ci}(X)\cos(X) + \sin(X)({\rm si}(X) - \frac{\pi}{2})\}\right], \tag{8}$$

where $X^2 = 6\mu_l/\mu_i$ and ci(X) and si(X) are the cosine and sine integrals.

Effect of thermal lattice expansion

Within the quasi-harmonic approximation [18], the Helmholtz free energy of a cubic crystal is given by [19]:

$$F(T,V) = U(V) + F^{\rm vib}(T,V) + F^{\rm el}(T,V), \tag{9}$$

where U is the static energy at 0 K, $F^{\rm vib}$ is the contribution due to lattice vibration and $F^{\rm el}$ the energy due to electronic thermal excitations. We rely on the adiabatic approximation to treat each term independently. The vibrational Helmholtz free energy per cell is given in the harmonic approximation by [19]:

$$F^{\rm vib}(T,V) = \frac{1}{2N}\sum_{\mathbf{q},\nu} \hbar\omega_{\mathbf{q},\nu}(V) + \frac{k_B T}{N}\sum_{\mathbf{q},\nu} \ln\left[1 - \exp\left(\frac{-\hbar\omega_{\mathbf{q},\nu}(V)}{k_B T}\right)\right], \tag{10}$$

where N is the number of $\mathbf{q}$-points, the first term is the contribution to the zero-point energy and the second term is the phonon contribution at finite temperature. $F^{\rm el}$ can be neglected as the band gap is much larger than thermal energies.

The energy minimum of $U(V) + F^{\rm vib}(T,V)$ at a given temperature corresponds to zero pressure and gives the variation of volume with temperature due to thermal expansion. To perform those calculations we used the `thermo_pw` code [20, 21]. The phonon frequencies were computed using the same LDA and PBE pseudopotentials as in the manuscript, without spin-orbit coupling, at nine different volumes. The resulting energies were fitted using the Murnaghan equation of state [22]. We used a 18×18×18 $\mathbf{k}$-point grid for the electron and a 6×6×6 $\mathbf{q}$-point grid for the phonons. The obtained volume variation is given in Fig. S4.

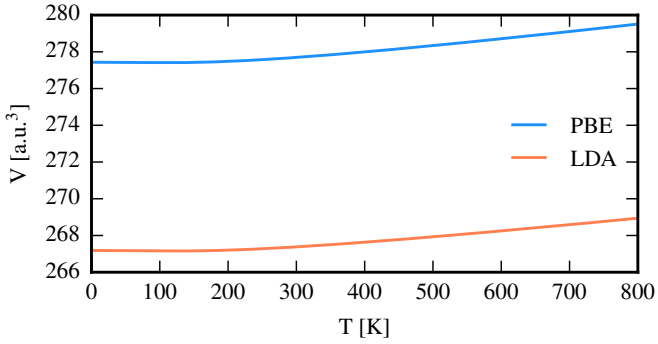

FIG. S4. Variation of volume with temperature due to thermal expansion using the LDA or PBE exchange correlation functionals.

The change of eigenenergies due to thermal expansion is given by [23]:

$$\Delta\varepsilon_{n\mathbf{k}}(T) = -\frac{\partial\varepsilon_{n\mathbf{k}}}{\partial P}\Big|_T \int_0^T dT' 3\alpha(T') B(T'), \tag{11}$$

where $B(T) = -V(\partial P/\partial V)_T$ is the bulk modulus and $3\alpha = V^{-1}(\partial V/\partial T)_P$ is the thermal expansion coefficient. B and α are obtained via numerical differentiation starting from the volumes calculated in the above figure.

We note that in Eq. 11 we carried the $\partial\varepsilon_{n\mathbf{k}}/\partial P$ term out of the temperature integral. This common temperature-independent approximation is valid in the elastic regime. To make sure that this approximation is

$\partial\varepsilon_{n\mathbf{k}}/\partial P$	LDA		PBE	
eV/Mbar	4 K	300 K	4 K	300 K
VBM	11.257	11.262	11.841	11.874
CBM	9.535	9.541	9.854	9.884
Ind. Gap	-1.722	-1.721	-1.987	-1.990

TABLE S3. Variation of the eigenenergies with pressure at two temperatures using the PBE and LDA pseudopotentials.

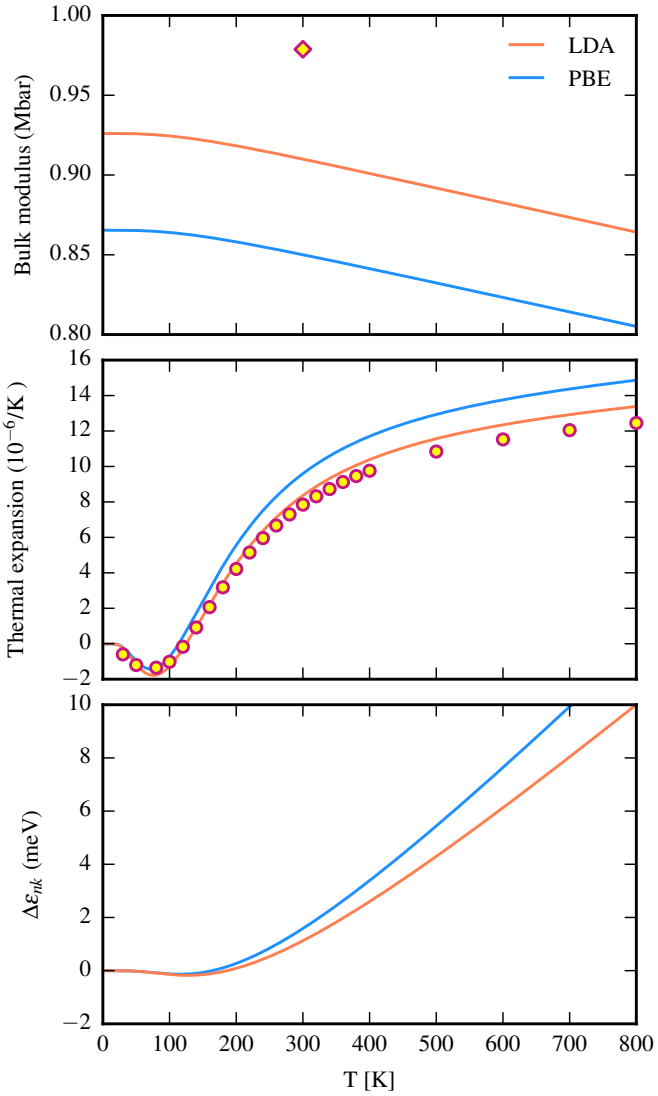

FIG. S5. Variation of the bulk modulus, the thermal expansion and eigenstates renormalization with temperature of silicon. Experimental values are from Refs. 24 (yellow diamond) and 25 (yellow dots).

valid, we compute $\partial\varepsilon_{n\mathbf{k}}/\partial P$ at 4 K and 300 K by numerical derivation around the equilibrium volume for that temperature. From Table S3 we see that indeed the temperature dependence is negligible and we therefore use the value at 4 K in Eq. 11.

The bulk modulus, the thermal expansion and eigenstates renormalization with temperature of silicon computed with the LDA and PBE exchange-correlation functionals are presented in Fig. S5. From the bottom panel we see that thermal lattice expansion leads to a slight increase of the band gap of silicon. For PBE, the valence band top and conduction band bottom change by -9.5 meV and -7.8 meV from 0 K to 300 K, therefore the net increase of the band gap is 1.7 meV. This variation is much smaller than the gap renormalization arising from electron-phonon interactions (as discussed next), therefore in the present case this effect can safely be neglected when calculating carrier mobilities.

Band	Direction	without e-ph interaction	with e-ph interaction	Variation
Light hole	[100]	0.334	0.342	+2%
	[111]	0.656	0.697	+6%
Heavy hole	[100]	0.334	0.343	+3%
	[111]	0.656	0.704	+3%
Split-off hole	[100]	0.218	0.220	+1%
	[111]	0.099	0.100	+1%
Electron	long.	0.927	0.966	+4%

TABLE S4. Effective masses of silicon computed at the LDA level without SOC, with or without the electron-phonon renormalization of the band structure at 0 K. The effective masses were obtained by using data from Ref. 26.

Electron-phonon renormalization of the bandstructures and free carrier screening

The electron-phonon renormalization of the bandstructure has been discussed for the case of silicon in considerable detail in Ref. 26. The calculated zero-point renormalization of the fundamental gap is -56.2 meV within the non-adiabatic Rayleigh-Schrödinger perturbation theory. This change corresponds to 5% of the band gap. We extracted the effective masses using data from that paper, and the results are shown in Table S4 for specific directions.

The electron-phonon renormalization of the bands leads to an increase of both electron and hole effective masses between 1% and 6%. Therefore, we can reasonably estimate that similar changes in effective masses will occurs in our calculations. Given the dependence of the mobility on effective mass, we estimate a 5% reduction in mobility due to this effect.

The effect of free carrier screening can be included via a Lindhard dielectric function using *ab initio* parameters as described in Ref. 27. In this case the screening only affects phonons with energy below the plasma energy of the doped carriers. For intrinsic silicon, which is the main focus of our work, the carrier concentration is below 10^{15} cm^{-3}. Using data from Ref. 28, we estimate

that the plasma energy in this case would be well below 0.1 meV, therefore the free carrier screening would be ineffective for nearly all phonons. We also mention that the renormalization of the band structure arising from the free carriers is negligible in this case [28].

* feliciano.giustino@materials.ox.ac.uk

[1] S. Baroni, S. de Gironcoli, A. Dal Corso, and P. Giannozzi, Rev. Mod. Phys. **73**, 515 (2001).
[2] S. Poncé, E. R. Margine, C. Verdi, and F. Giustino, Computer Physics Communications **209**, 116 (2016).
[3] P. Bratley and B. L. Fox, ACM Trans. Math. Softw. **14**, 88 (1988).
[4] H. S. Hong and F. J. Hickernell, ACM Trans. Math. Softw. **29**, 95 (2003).
[5] C. H. Rycroft, Chaos **19** (2009).
[6] M. Rohlfing and S. G. Louie, Phys. Rev. B **62**, 4927 (2000).
[7] G. Dresselhaus, A. F. Kip, and C. Kittel, Phys. Rev. **98**, 368 (1955).
[8] P. Y. Yu and M. Cardona, *Fundamental of Semiconductors*, edited by H. E. Stanley and W. T. Rhodes (Springer, 2010).
[9] R. N. Dexter and B. Lax, Phys. Rev. **96**, 223 (1954).
[10] S. Sze and K. K. Ng, *Physics of semiconductor Devices - Third Edition* (Wiley, 2007).
[11] J. Bardeen and W. Shockley, Phys. Rev. **80**, 72 (1950).
[12] M. S. Hybertsen and S. G. Louie, Phys. Rev. B **35**, 5585 (1987).
[13] R. Resta, Phys. Rev. B **16**, 2717 (1977).
[14] H. Brooks, Phys. Rev. **83**, 879 (1951).
[15] S. S. Li and W. R. Thurber, Solid-State Electronics **20**, 609 (1977).
[16] M. Balkanski and R. F. Wallis, *Semiconductor Physics and Applications* (Oxford University Press, 2000).
[17] P. Norton, T. Braggins, and H. Levinstein, Phys. Rev. B **8**, 5632 (1973).
[18] S. Baroni, P. Giannozzi, and E. Isaev, Rev. Miner. Geochem. **71**, 39 (2010).
[19] M. Palumbo and A. D. Corso, Journal of Physics: Condensed Matter **29**, 395401 (2017).
[20] http://people.sissa.it/∼dalcorso/thermo_pw_dist.html, .
[21] A. D. Corso, Journal of Physics: Condensed Matter **28**, 075401 (2016).
[22] F. D. Murnaghan, Proc. Natl. Acad. Sci. USA **30**, 244 (1944).
[23] P. Lautenschlager, P. B. Allen, and M. Cardona, Phys. Rev. B **31**, 2163 (1985).
[24] H. J. McSkimin and P. A. Jr., Journal of Applied Physics **35**, 2161 (1964).
[25] Y. Okada and Y. Tokumaru, Journal of Applied Physics **56**, 314 (1984).
[26] S. Poncé, Y. Gillet, J. Laflamme Janssen, A. Marini, M. Verstraete, and X. Gonze, J. Chem. Phys. **143**, 102813 (2015).
[27] C. Verdi, F. Caruso, and F. Giustino, Nature Communications **8**, 15769 (2017).
[28] F. Caruso and F. Giustino, Phys. Rev. B **94**, 115208 (2016).